Rapid assessment of riverine flood inundation in Chenab floodplain using remote sensing techniques

Asif Sajjad[1*], Jianzhong Lu[2], Xiaoling Chen[2], Chikondi Chisenga[3] and Nausheen Mazhar[4]

Abstract

Introduction After flood occurrences, remote sensing images provide crucial information for mapping flood inundation extent. Optical satellite images can be utilized to generate flooded area maps when the flooded areas are free from clouds.

Materials and Methods In this study flooded area was calculated using a variety of water indices and classification algorithms, calculated on Landsat data. Pre-flood, during flood, and post-flood satellite data were collected for in-depth flood investigation. The delineation of inundated areas was done using the Normalized Difference Water Index (NDWI), Modified Normalized Difference Water Index (MNDWI), and Water Ratio Index (WRI). In order to detect and compare flooded areas with water indices, the supervised maximum likelihood algorithm was also used for land use and land cover mapping.

Results The results of the investigation allowed for a flooded area and recession. The analysis revealed that the flooded area covered about 68% of the study area, and remained standing for seven weeks. We used the misclassified areas approach, as determined, using the classified results, to improve the results of the flooded areas, generated through the use of each of the 3 water indices. The result showed that the MNDWI images showed better accuracy of above 90%, which reflects the reliability of the results.

Conclusion This proposed remote sensing (RS) technique provides a basis for the identification of inundated areas with less misclassified areas, which enable an emergency response to be targeted, for newly flooded areas. Thus, the present study provides a novel rapid flood mapping perspective and provides a considerable contribution to flood monitoring.

Keywords Riverine flood, Rapid flood mapping, Water indices, Optical satellite data, Flood monitoring

*Correspondence:
Asif Sajjad
asifsajjad@qau.edu.pk
[1] Department of Environmental Sciences, Faculty of Biological Sciences, Quaid-I-Azam University, Islamabad 45320, Pakistan
[2] State Key Laboratory of Information Engineering in Surveying, Mapping and Remote Sensing, Wuhan University, Wuhan 430079, China
[3] Department of Earth Sciences, Ndata School of Climate and Earth Sciences, Malawi University of Science and Technology, Box 5196, Limbe, Malawi
[4] Department of Geography, Lahore College for Women University, Lahore 54000, Pakistan

Introduction

Floods are the most prevalent natural disaster in the world, having a tremendous potential for devastation (Kundzewicz et al. 2014; Arnell and Gosling 2016). In recent decades, the frequent occurences of several floods have had severe impacts on the humans, and key resources around the world (Uddin et al. 2019; Sivanpillai et al. 2021). Although this devastating flood disaster cannot be completely avoided, the consequences can be mitigated by using efficient rapid flood risk reduction measures that incorporate remote sensing (RS). RS

Sajjad *et al. Geoenvironmental Disasters*   (2023) 10:9

Page 2 of 18

technology is the most cost-effective method providing rich information of all phases of flood disaster, which may be utilised for instant rapid flood mapping (RFM) (Zhang et al. 2015; Khalid et al. 2018). There are burgeoning studies where RFM has been applied for identifying flooded areas and providing reliable information for early flood response (Islam et al. 2010; Haq et al. 2012). These actions require up-to-date satellite data for flood mapping, as many floods last for several days (Refice et al. 2014; Munasinghe et al. 2018; Sajjad et al. 2020). Previous studies have analyzed the potentials of various RS techniques for accurate flood mapping (Gao et al. 2018; Uddin et al. 2019; Sivanpillai et al. 2021). Optical RS data, which provide up-to-date information with a high temporal resolution for public users, has been widely used in the detection of flooded areas during the flood event (Alphan et al. 2009; Roni et al. 2014; Goffi et al. 2020). On the other hand, the presence of clouds, lowers the availability of optical RS images during flooding, which has an impact on overall flood mapping. Synthetic Aperture Radar (SAR) images, which can pierce clouds and obtain images in all weather situations, are commonly employed for flood mapping under these circumstances (Joyce et al. 2009; Manavalan 2017; AlFaisal et al. 2018).

SAR data are normally very expensive and difficult to process (Boni et al. 2016). Furthermore, SAR satellite provides free data in some regions through certain agencies, such as Sentinel Asia, and global charter on flood disasters (Kaku et al. 2015). With the availability of Sentinel-1 data, some studies have utilized it for flood mapping (Rahman and Thakur 2017; Amitrano et al. 2018; Borah et al. 2018; Uddin et al. 2019).

In our study, however, flooded areas were cloud free, because the causal rainfall event happened in the upper Chenab river roughly 10 days before the major flood water reached the selected Chenab floodplain. Cloud-free optical images have been found to be excellent for RFM in previous researches (Revilla-Romero et al. 2015; Rosser et al. 2017; Sajjad et al. 2019).

The optical RS has provided a wide source of reliable data, which is significant for a detailed RFM. Furthermore, the frequency of optical satellites collecting images has possessed a high possibility of obtaining more post-flood images (Notti et al. 2018; Giordan et al. 2018). Thus, the flood maps can be updated more frequently using multispectral data. The Landsat-8 images are the primary source of multispectral data used in this work (Sanyal and Lu 2004; Wulder et al. 2012). The study area in our case is situated on two neighbouring Landsat satellite Paths (150 and 151), allowing us to acquire images with an 8-day temporal resolution. This enabled us to carry out in-depth RFM in the study area.

In most situations, RFM is based on water indices that use band ratios generated from satellite spectral data and threshold values applied to the ratios to extract flooded areas (Revilla-Romero et al.2015; Sajjad et al. 2021). RS-based water indices are utilized for the extraction of flooded areas, including the Normalized Difference Water Index (NDWI) (McFeeters 1996), which uses reflected NIR and Green bands for water area assessment, and the Modified NDWI (MNDWI) (Xu 2006), which uses the SWIR band and the Green band to enhance water areas while removing built-up and vegetation area noise. Although NDWI results occasionally mix with built-up, it does give better flood inundation results in vegetation areas, in some circumstances. According to Rokni et al. (2014), it performed better than the MNDWI in Lake Urmia in Iran, which has no built-up areas. In the NDWI, water features have positive values, whereas vegetations and soil have negative values. However, when the MNDWI is used in water regions with built-up, the MNDWI image shows positive values. Thus, it becomes apparent that both the indices have a limitation for flood mapping as they both rely on environment i.e., whether-built up or vegetation is present in the study site. In the present study, mixed land cover dominates most river bank environments where the built-up area can be seen along with cultivated land, which means that relying on merely one type of index, may not be suitable for accurate RFM.

Therefore, the main goal of the present study is to delineate rapid flooded areas using suitable water indices. Results from the water indices, propose a step-wise approach for accurately performing RFM, in an environment where built-up and vegetation land uses are mixed. Such an approach gives an insight to the flood situation in this significant riverine floodplain with minimum inclusion of other non-water classes. Also, in case of flood disaster occurrence, such an insight can assist in proper decision making for emergency flood management.

Materials and methods
Study area
The research is being carried out in the Chenab Basin, Pakistan which stretches from 70°41′13″ to 71°37′59″ E and 29°6′0″ to 30°31′34″ N (Fig. 1). Every year, riverine floods occur in this fertile flood-prone Chenab Basin of Pakistan. We have chosen a 120-km stretch of the Chenab River as the focus of our research (Fig. 1). Its spatial extent is between Head trimmu in north to Head Panjnad in the south. Chenab river is 272 km long (within Pakistan boundary), and its total catchment area is 41656 km^2. Amongst these 41,656 km^2, 27,195 km^2 of the catchment area, lies in the mountainous region, that is located upstream Head Marala, and this area remains
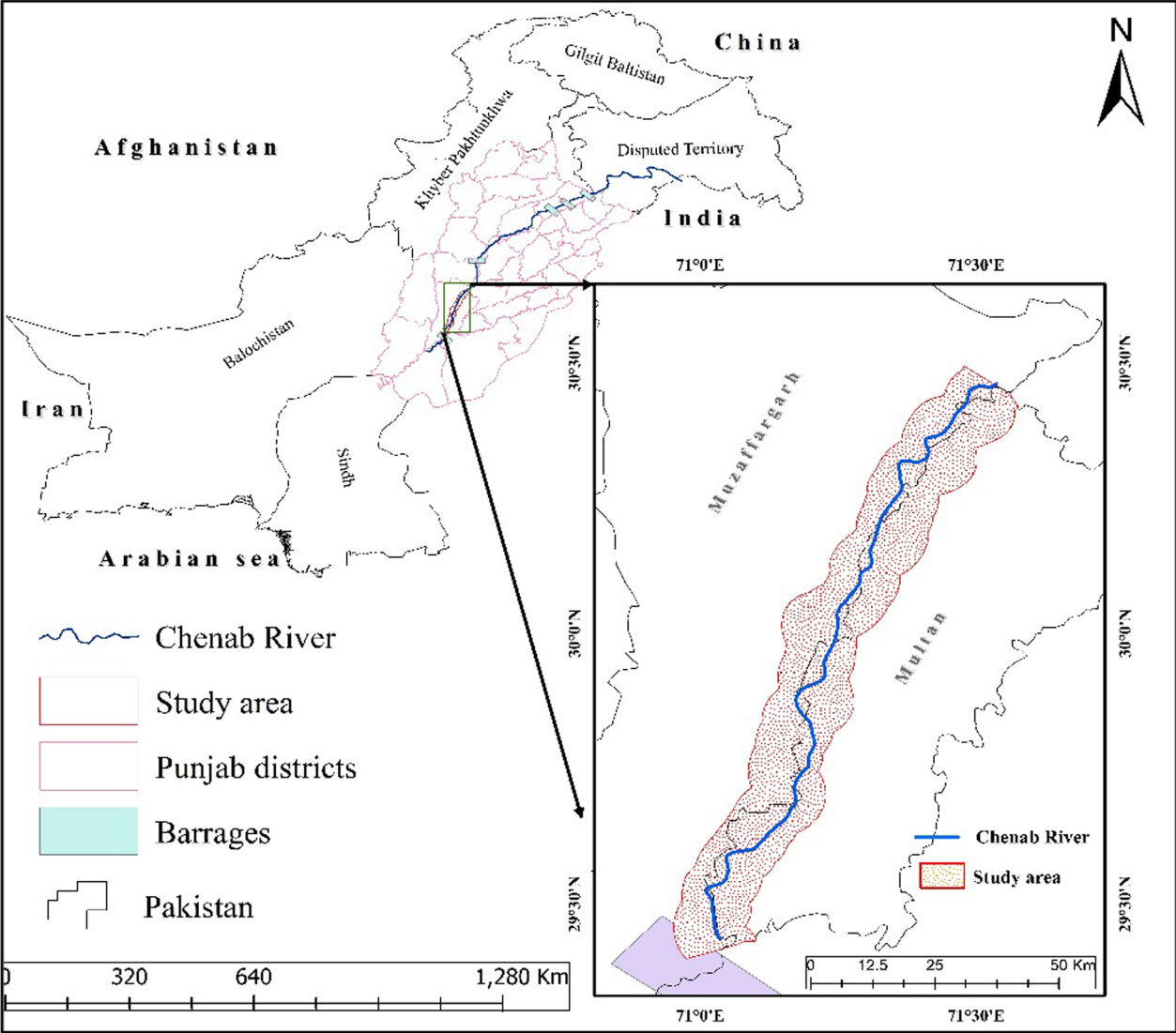
Fig. 1 The Chenab River and the study area's location

a frequent victim of flash floods, whereas, the riverine floods, remain a characteristic of the low lying areas (Mahmood and Rani 2022). The study area has an arid type of climate with hot and dry summers while cold and dry winters.The average annual rainfall is 157 mm, with July recording the highest total of 50 milimeters and October recording the lowest total of 2 milimeter (PMD 2014). The locals are engaged with agriculture as the primary economic activity of this region. Riverine floods have often caused devastation in the study region, but the 2014 flood, which triggered more human life losses and economic damages than any other flood since 1992, which was the deadliest in the flood history of this region. The study area has characterized with a flat, alluvial plain

Table 1 Characteristics of Landsat 8 (OLI) images used in the present study

Landsat Paths	Rows	Dates	Flood stages
151	39	08-09-2014	Pre flood
150	39,40	17-09-2014	During flood
151	39	24-09-2014	During flood
150	39,40	03-10-2014	During flood
151	39	10-10-2014	Post flood
150	39,40	19-10-2014	Post flood
151	39	26-10-2014	Post flood
151	39	11-11-2014	Post flood

productive land, with orchards and deserts on all sides (FFCI 2014).

Materials

The Landsat 8 images were obtained from the US Geological Survey's database. We used eight Landsat images taken between September 8th and November 11th, 2014. (Table 1). Spatial ground truth datasets were also collected through Google Earth (GE) platform, which were utilised to validate land use and land cover (LULC) classification (Hu et al.2013). In addition, GE images of flood stages were also obtained (with acquisition dates corresponding to the Landsat-8 images) for comparison with Landsat-based LULC classification and flood mapping. The closest available pre-flood GE image with used Landsat image was taken on 4th August 2014, during-flood images on 18th September 2014, 1st October 2014 and the post-flood image on 11th November 2014.

Methods

To prepare the satellite images for further processing, radiometric calibration, atmospheric correction, and layer mosaicking were used as pre-processing procedures. To convert satellite images to satellite radiance, the Landsat radiometric calibration method in ENVI 4.8 was used to perform radiometric calibration and atmospheric correction (Khalid et al.2018). Every Landsat image's digital number values were transformed to reflectance after being converted to satellite radiance (Chavez 1996). Layer stacking and mosaicking were performed using the spatial analysttool in Arc GIS. The final Landsat images were used for LULC mapping based on ML classification in order to estimate flooded areas extent using water indices, as shown in Fig. 2. Classes of water, vegetation, built-up, sand, and barren areas were identified. A total of 120 GE training points were obtained to facilitate the ML classification for LULC mapping. These points were digitized and imported in the Arc GIS 10.5, for further mapping. Later, the LULC map was converted into vector shapefile format and used for spatial overlay technique. This enables us to spatially intersect all land uses in order to compare classified map results to flood inundation outcomes in a consistent manner.

We also used the following water indices; MNDWI, NDWI and WRI, to extract the flood water areas. The NDWI index is effective for detecting flood water (McFeeters 1996), as it makes use of the robustness in water absorption and reflection of vegetation in Near infra-red (NIR) bands and high reflection of water spectral signature in the Green band (McFeeters 1996). Green (band 3) and NIR (band 5) are used to determine the NDWI, as shown in Eq. (1):

$$NDWI = \frac{\text{Green(band3)} - \text{NIR(band5)}}{\text{Green(band3)} + \text{NIR9band5)}} \qquad (1)$$

The ability of this index to distinguish between water and vegetation is very strong. However, if there is a built-up environment in water areas, its efficiency is lowered. Therefore, Xu (2006) proposed the MNDWI index to overcome this limitation, which effectively distinguishes water from built-up areas. Green (band 3) and Shortwave infrared (SWIR) (band 6) are used to calculate the index, as shown in Eq. (2):

$$MNDWI = \frac{\text{Green(band3)} - \text{SWIR(band6)}}{\text{Green(band3)} + \text{SWIR(band6)}} \qquad (2)$$

Shen and Li (2010) define WRI as the ratio of total spectral reflectance in the Green (band 3) and Red (band 4) to NIR (band 5) and SWIR (band 6) wavelengths (band 6). As indicated in Eq. (3), the ratio is calculated:

$$WRI = \frac{\text{Green(band3)} + \text{RED(band4)}}{\text{NIR(band5)} + \text{SWIR(band6)}} \qquad (3)$$

In the case of flood map generation, however, the manual threshold-based technique appears to be accurate. This method often identifies consistent water areas (Manjusree et al.2012). Similar to the study by Acharya et al. (2018), this present study performedflood mapping technique, in which each index was given manually selected threshold values from -1 to $+1$ for distinguishing the results of the analysis for each image into two categories: water and non-water pixels. Furthermore, the suitable manual threshold value for getting the high overall accuracy has been obtained by applying the trial-and-error method and comparing it to a reference classified map and visual interpretation. For comparison with water indices, we compared index-based flooded areas, as an area that experienced flooding. On during flood classified images, MNDWI, NDWI and WRI indices were applied to present the area under flood. The classified image was utilized as a reference image. Afterwrds, spatial overlay change detection analysis was applied to evaluate misclassified water areas, calculated by the indices.

Inundation maps and classsified images validation

The validation of flood inundation maps and LULC classified image was performed using the GE platform. The Arc GIS spatial analyst's random sample points tool was used to obtain random sample points on the classified image. After that, the points were transformed to a kml format and overlaid on the GE platform. Visual interpretation and native knowledge were used to assess the accuracy value of these 150 points on a classified image.
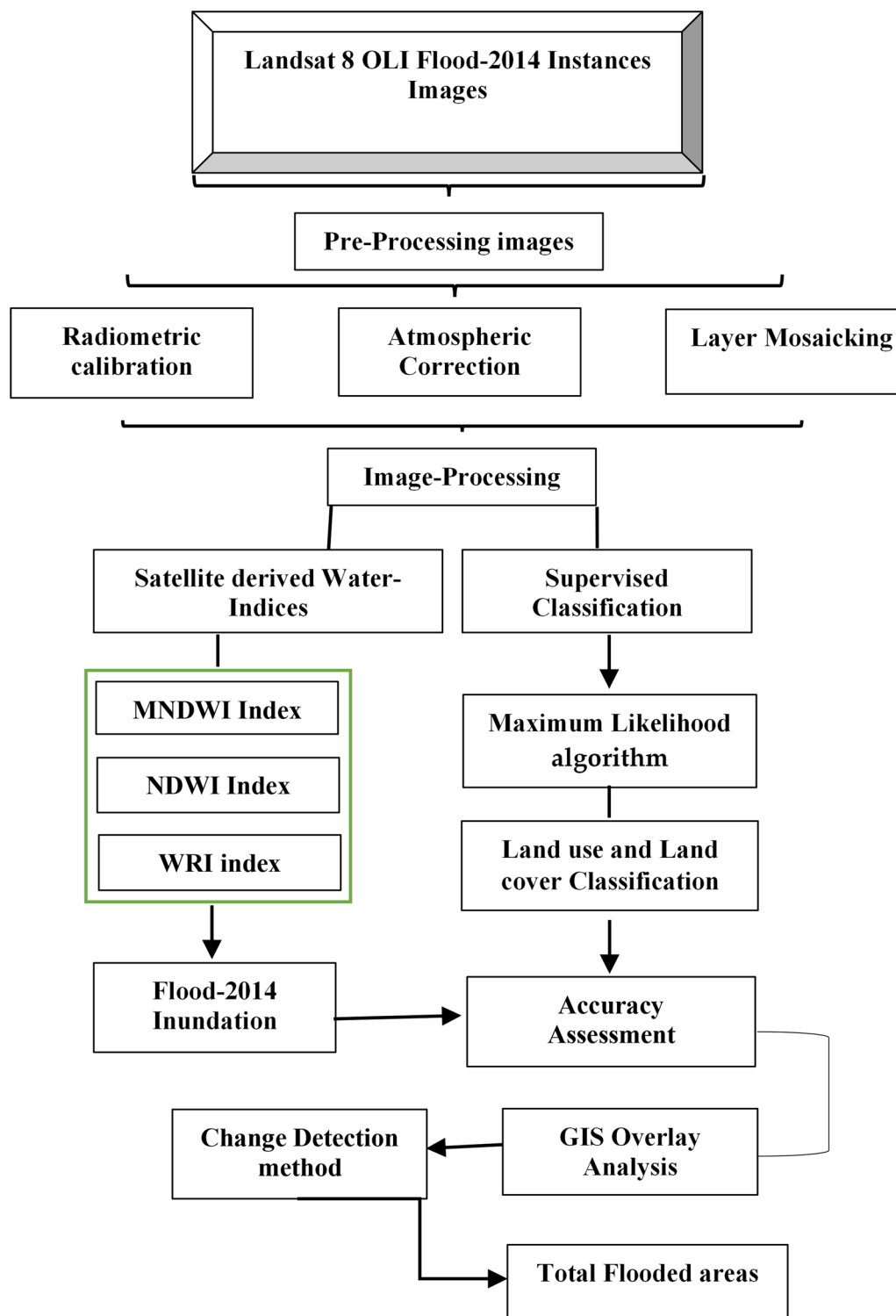
Sajjad *et al. Geoenvironmental Disasters*   (2023) 10:9

Page 5 of 18

Fig. 2 Methodological outline for RFM using Landsat-8 flood images

A total of 30 Arc GIS random points were applied for each class, including water, vegetation, built up, sand and barren areas on classified image.

Similarly, the validation of inundation maps was also assessed through better resolution GE digitized points. As such, the during flood 17th September inundation

Sajjad *et al. Geoenvironmental Disasters*   (2023) 10:9

Page 6 of 18

maps were validated, utilizing corresponding 18th September during flood GE image based digitized points. Likewise, the validation of remaining flood inundation maps was also assessed based on GE points. The water/not water classifications of these points were observed for accuracy assessment. If a reference point was interpreted as 'non-water' in the pre-flood stage but as 'water' in the post-flood stage, it was evaluated as a flooded class. Reference data was interpreted as 'non-water' class if they were interpreted as 'non-water' in pre-flood and 'non-water' in post-flood stages. The accuracy of flood maps and validation of water and non-water classes were assessed using a total of 800 GE digitized points,

100 points for each image. Furthermore, we used the Confusion matrix for the final accuracy results through comparison of the RFM image points with GE source points. The resultant flood maps were used to calculate overall, producer, and user accuracies. Overall accuracy is assessed through the ratio of corrected points of final images with the total number of GE reference points. User accuracy is obtained by separating corrected points of RFM with the total validation points of a specific class, whereas producer accuracy is calculated by computing the corrected RFM points for each class (Sajjad et al. 2020; Sivanpillai et al. 2021). The Kappa coefficient was also applied to confirm the agreement, as positive or

Table 2 Overall accuracy assessment and Kappa coefficient values of RFM produced by used water indices

Landsat-8 images	Overall accuracy			Kappa values		
	MNDWI	NDWI	WRI	MNDWI	NDWI	WRI
08/09/2014	0.91	0.89	0.87	0.86	0.80	0.77
17/09/2014	0.93	0.88	0.85	0.87	0.77	0.71
24/09/2014	0.97	0.90	0.78	0.93	0.81	0.63
03/10/2014	0.95	0.88	0.89	0.90	0.77	0.78
10/10/2014	0.90	0.87	0.87	0.80	0.78	0.76
19/10/2014	0.95	0.90	0.79	0.89	0.83	0.65
26/10/2014	0.90	0.87	0.84	0.80	0.76	0.70
11/11/2014	0.96	0.92	0.88	0.91	0.85	0.77

Table3 User and producer accuracy of RFM generated from used water indices

Landsat-8 images	Producer accuracy			User accuracy		
	MNDWI	NDWI	WRI	MNDWI	NDWI	WRI
Water class						
08/09/2014	0.91	0.88	0.75	0.93	0.88	0.87
17/09/2014	0.91	0.87	0.76	0.95	0.85	0.91
24/09/2014	0.94	0.86	0.74	0.99	0.92	0.76
03/10/2014	0.91	0.89	0.77	0.95	0.86	0.90
10/10/2014	0.90	0.88	0.81	0.86	0.87	0.91
19/10/2014	0.97	0.90	0.75	0.91	0.92	0.95
26/10/2014	0.90	0.88	0.80	0.87	0.84	0.90
11/11/2014	0.99	0.85	0.81	0.99	0.92	0.91
Non-Water class						
08/09/2014	0.93	0.86	0.93	0.92	0.92	0.85
17/09/2014	0.95	0.88	0.93	0.91	0.92	0.79
24/09/2014	0.99	0.91	0.81	0.95	0.88	0.78
03/10/2014	0.96	0.87	0.97	0.94	0.91	0.84
10/10/2014	0.92	0.92	0.91	0.93	0.92	0.86
19/10/2014	0.93	0.93	0.96	0.98	0.91	0.90
26/10/2014	0.91	0.86	0.92	0.91	0.91	0.78
11/11/2014	0.99	0.96	0.93	0.94	0.93	0.84

Sajjad *et al. Geoenvironmental Disasters*   (2023) 10:9

Page 7 of 18

negative, between resulted inundation maps with reference points.

Results

Accuracy assesment

Tables 2 and 3 show the accuracy of the MNDWI, NDWI, and WRI indices for all of the images.The analysis shows that overall accuracy (OA) and Kappa coefficient (KC) values calculated for RFM produced from MNDWI resulted images were higher than those produced from NDWI and WRI images (Table 2). The overall MNDWI derived inundation accuracy of six images was above 90%, and only two images had values of 90%, as shown in Table 2. Similarly, the KC values were higher than 0.80 for six MNDWI derived images and for three NDWI images. Furthermore, the highest overall accuracy of 97% was obtained by the MNDWI index from 17th September image, while 96% from 11th November images. Additionally, the highest attained overall accuracy of the NDWI index was 92% calculated from the 11th November image, while the WRI index image of 03rd October, achieved the highest accuracy of 89%. The detail about overall accuracy and KC values are listed in Table 2.

RFM derived from the NDWI index presented some instances when non-flooded water areas were misclassified as flooded areas. On the contrary, WRI index results proved that in some areas the flooded areas were misidentified as non-flooded areas, resulting from the misclassification of various pixels. The flood map must have the most accurately identified flooded area pixels in order to generate reliable RFM maps for emergency flood response and recovery. In our study, the producer accuracy (PA) values for the flood water class of MNDWI derived images were higher than the NDWI and WRI resulted images (Table 3). The PA values for the flood water class of all MNDWI images were above 90%, which resulted in the maximum correctly classified flooded areas. In comparison, the PA values of all NDWI images were below 90% and all WRI images had PA values less than 82%. Similarly, the user accuracy (UA) values associated with floodwater class were also higher in all MNDWI images than the NDWI and WRI images. Based on PA and UA results, the MNDWI index correctly identified relatively more floodwater areas than the NDWI and WRI. The PA and UA values for the non-water class were also higher in all MNDWI images, than they were in NDWI and WRI images. In the two images of 10th and 19th October, the NDWI, PA values were similar to the MNDWI. Likewise, the UA values associated with non-water class were maximum in all MNDWI images, compared to NDWI and WRI derived images.

Based on PA and UA values, results for the non-water class were higher in the MNDWI derived images than the following corresponding NDWI and WRI derived images. Furthermore, it was revealed from this study that MNDWI resulted images could be more reliable comparatively for generating RFM, in the post-disaster phase. Moreover, the NDWI results for some images were also acceptable, as they presented good accuracy. However, the WRI technique presented poor accuracy results and also mixed several floodwater areas into non-water areas. Furthermore, the detail about PA and UA values of MNDWI, NDWI and WRI are listed in Table 3.

Rapid flood mapping using different water indices

The flooded areas of riverine flood-2014 were delineated using different water indices to estimate the flood inundated and affected areas in the study area. Figures 3,4 and 5 depict the flooded areas, with the highest flood peak occurring on 17th September and remaining constant until 24th September. Later, water from the flooded areas regularly receded till 11th November 2014. Figure 7 and Table 2 show that rapid flood images obtained from the MNDWI index caught flooded areas substantially more closely and with high accuracy than NDWI and WRI derived images. The analysis revealed that the NDWI index resulted images were misclassified as some non-flooded barren land areas, located in the upper and lower part of the study area, were presented as flooded areas in all images (Fig. 4). On the other hand, the analysis showed that the WRI index could not detect floodwater areas accurately, as in some instances, it misclassified floodwater areas into non-flooded areas, which reduced the overall and user accuracy of the final images, as shown in Fig. 5 and Tables 2,3. Furthermore, the MNDWI derived image reveals that the highest peak-flood inundation of 17th September covered an area of 1023.4 km^2 (Fig. 3), while the NDWI index revealed the total of 1035 km^2 area was flooded (Fig. 4) and the WRI revealed the peak flood covered an area of 860 km^2 (Fig. 5). Similarly, in the 24th September image, the MNDWI index showed the total of 1000 km^2 area was under floodwater, whereas the NDWI index revealed the floodwater covered an area of 1005 km^2, and the WRI index indicated the total of 820 km^2 area was flooded. Further, the detail of rapid flood inundation mapping of all images is shown in Figs. 3,4,5 and 6. The maps produced by the MNDWI index, delineated flooded areas with high overall accuracy and could be used to permit flood emergency response actions in order to reduce flood impacts in future flood events.

In all images, the flood inundated areas retreated in three stages: In the first stage, a retreat from peak-flood, was identified in the South region, from 17th September
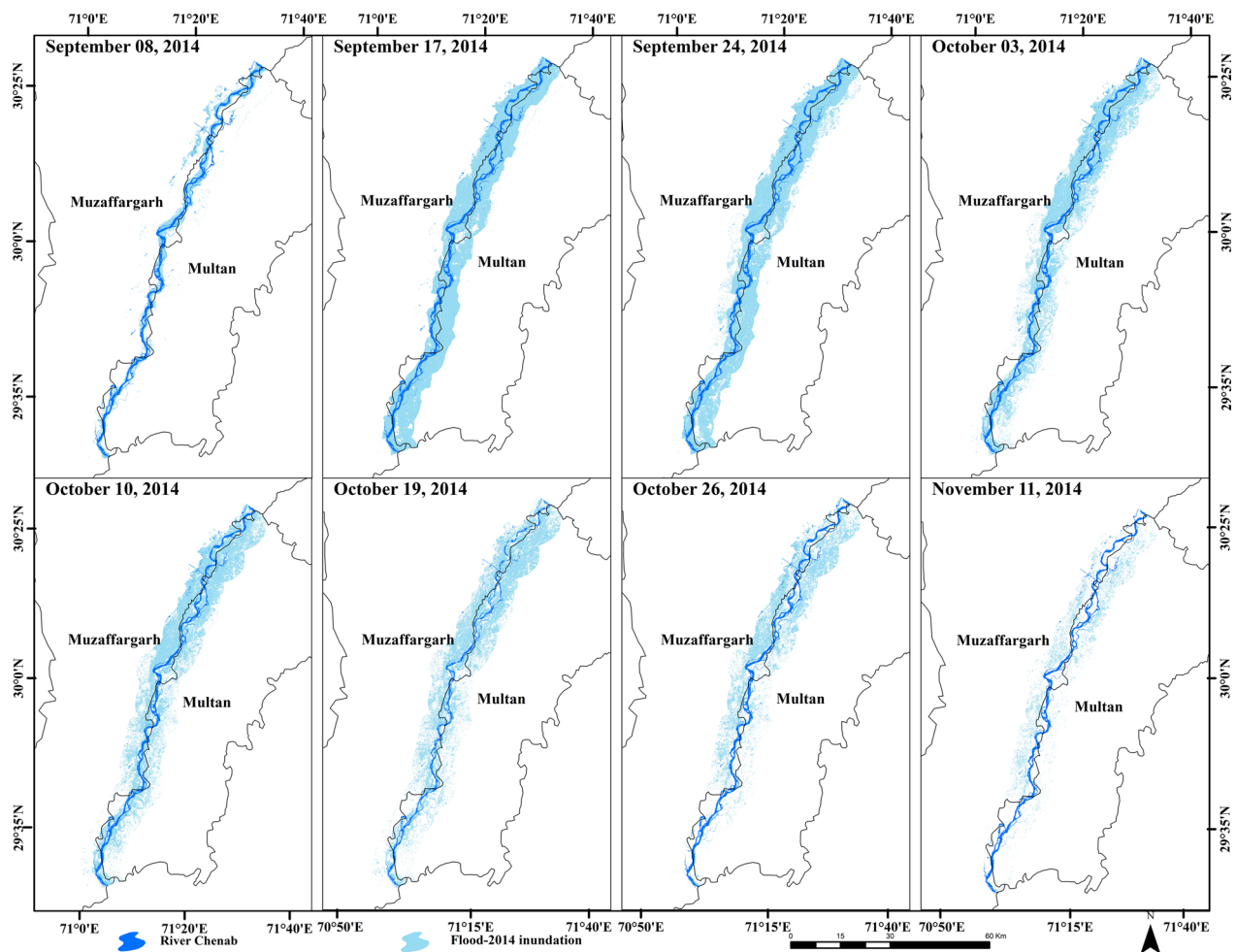
Sajjad *et al. Geoenvironmental Disasters*   (2023) 10:9

Page 8 of 18

Fig. 3 Spatio-temporal flooded areas extent from pre-flood to post-flood using MNDWI index

image to 10th October image. In the second phase, middle parts had started to experience decrease in standing flood water extent, till 26th October, and in the last stage, entire flood inundated water areas had retreated, in the post-flood 11th November 2014 image (Figs. 3,4,5). Later, all images of flood inundation revealed the same pattern of inundation when compared to better GE images (Fig. 7).

The RFM images and GE images (Fig. 7) reveal a similar flooded area spatial and temporal pattern from a pre-flood to a post-flood instance. The Chenab river was at a normal stage in the pre-flood instance, as seen in Fig. 7A. However, in the peak-flood 18th September GE image, the massive flooded areas along the Chenab river can be clearly seen. Similarly, the slight flood water changes are observed on the 1st October GE image (Fig. 7C), but it also shows the significant flooding in all the surrounding vegetation and settlement areas. As revealed in Fig. 7D, river Chenab has regained its pre-flood situation, as the flooded area was receded and a large quantity of soil

deposited material was found along the river basin. These results are consistent with those, calculated from water indices, as shown in Figs. 3, 4 and 5.

The overall accuracy of peak flood classified image was 92% and the KC accuracy of 88%, as shown in Table 4. Water (98%) and barren areas (99%) also had the highest user accuracy, as indicated in Table 4. The water class, with a 92% accuracy rate, likewise had the highest producer accuracy. The accuracy result indicates that the during flood classified image is suitable for further comparative intersection analysis.

Figure 8 reveals the supervised classified result for land use and land cover of during flood (17th September 2014) image. The result shows that flood caused a massive inundation which resulted in water class almost covering 60% of the total area. Whereas, the vegetation and built-up areas covered 22.40% and 11.85% respectively. The sand class covered only 1.1% and the barren area was only 4% of the total area. Hence, the massive floodwater
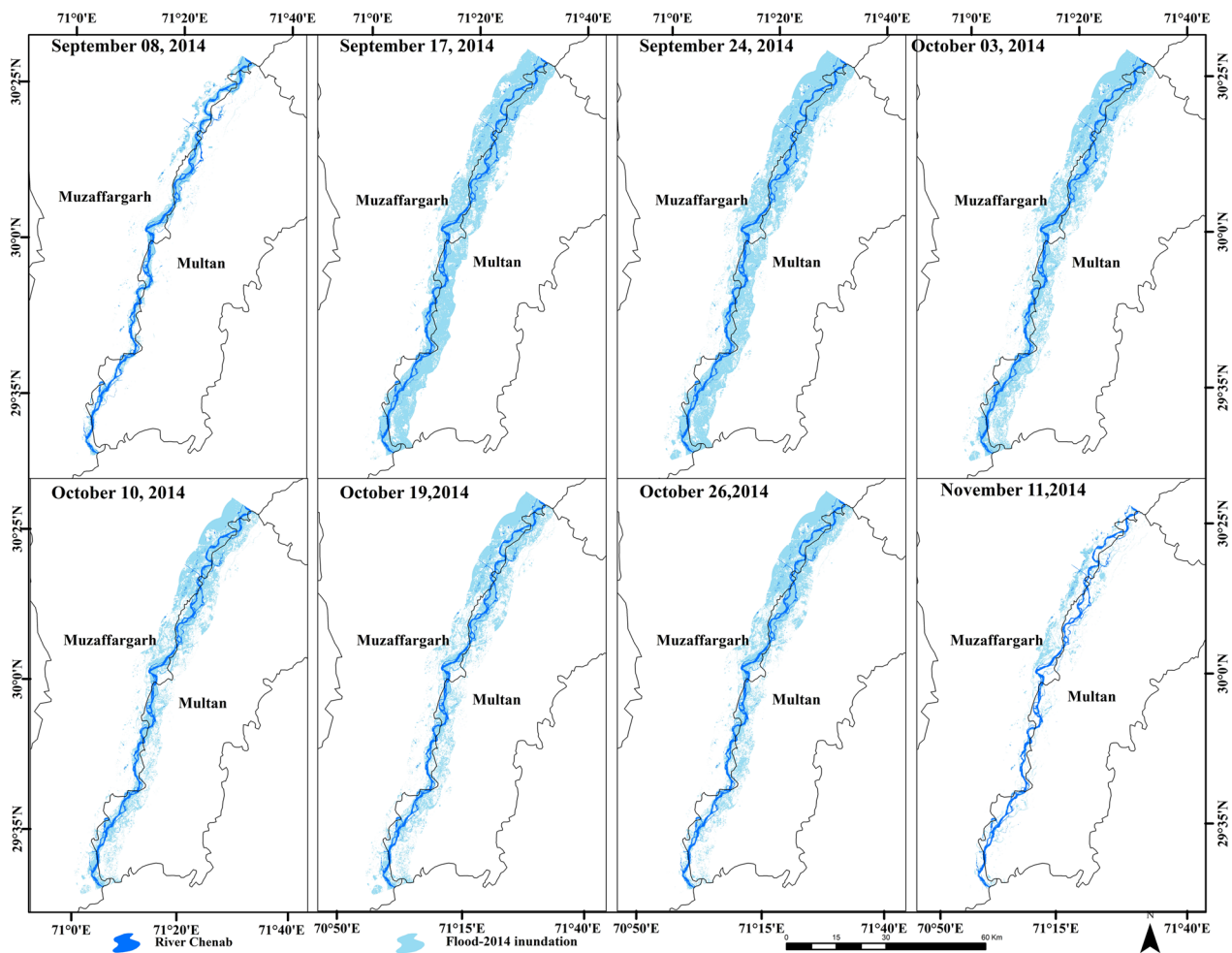
Fig. 4 Spatio-temporal flooded areas extent from pre-flood to post-flood using NDWI index

caused a large extent of agricultural and built-up areas to be flooded and registered damages to the standing crops and built-up environment.

In addition, the results of the during flood-2014 images are compared and intersected, as shown in Figs. 8 and 9. In Fig. 8, the classified image and images of water indices reveal the accumulated peak flood (17th September) extent. The classified image (Fig. 8A) shows the accumulated flooded area of 1005.4 km². While, the MNDWI image (Fig. 8B) reveals that a total area of 1023.4 km² was flooded, which shows very little difference from the classified image. Furthermore, the NDWI result shows that about 1035.1 km² area was under floodwater, which represents the highest flood inundated area if compared with other indices. As such, The WRI index result reveals that the floodwater covered an area of 860.04 km². Later, the comparative analysis reveals that the MNDWI image and classified

image are somehow supporting each other as shown in Figs. 8 and 9. Thus, our results suggest that the MNDWI index and Supervised ML classification can be used for rapid flood mapping in such areas for early flood response and operations. Furthermore, these flooded area results, when interpreted with the GE images (Fig. 7) obtained for almost the same dates as the used Landsat images, also revealed to some extent, the similar flood inundated areas, which further validated our flooded area extent, and also confirming that the flood inundation remained for about seven weeks and retreated slowly.

Comparing of water indices

We compared the results from supervised classification with the indices to determine how accurate are the mapped flooded areas when compared to the actual flooded area. In Fig. 10A, the supervised classified image was used as a reference. Then water indices-based
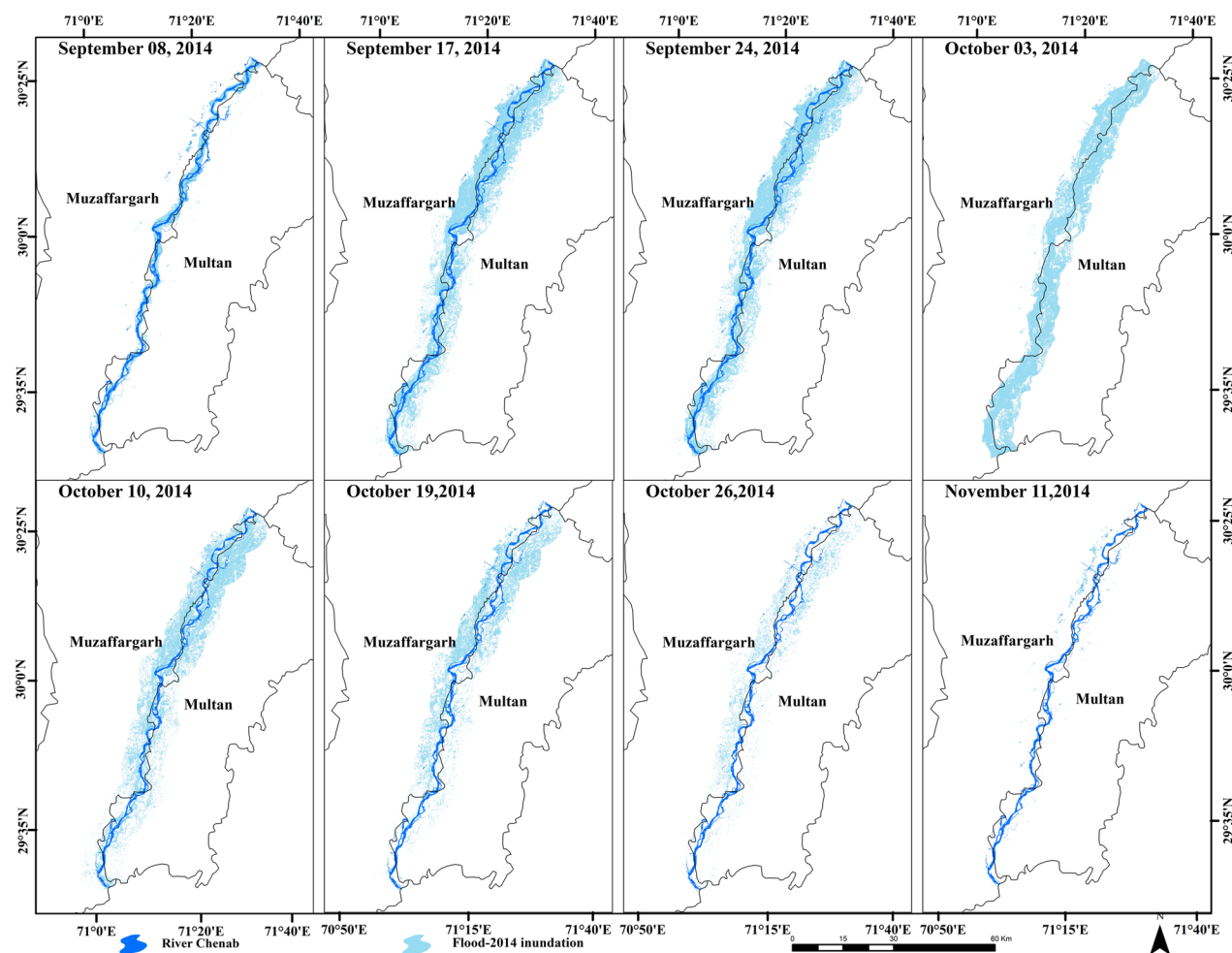
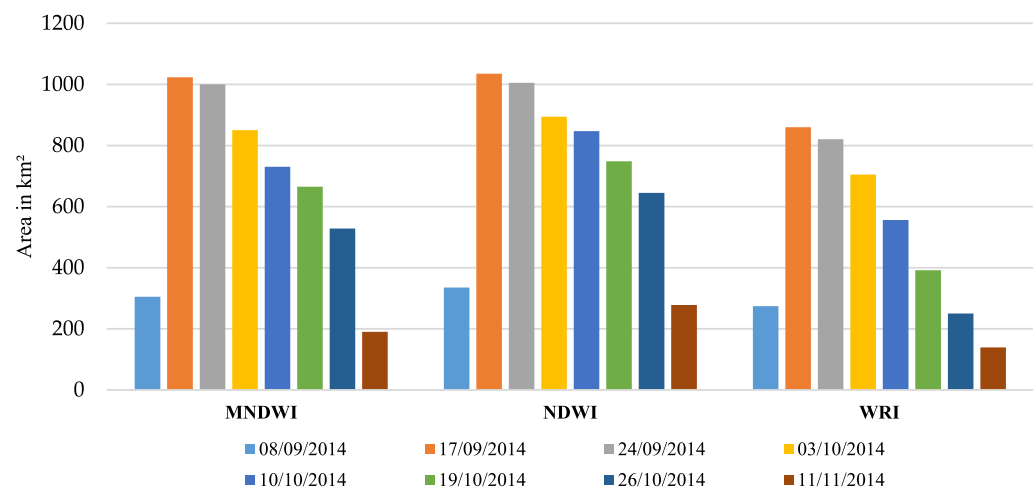**Fig. 5** Spatio-temporal flooded areas extent from pre-flood to post-flood using WRI index

Fig. 6 Flood inundated areas calculated using MNDWI, NDWI, and WRI indices on different dates
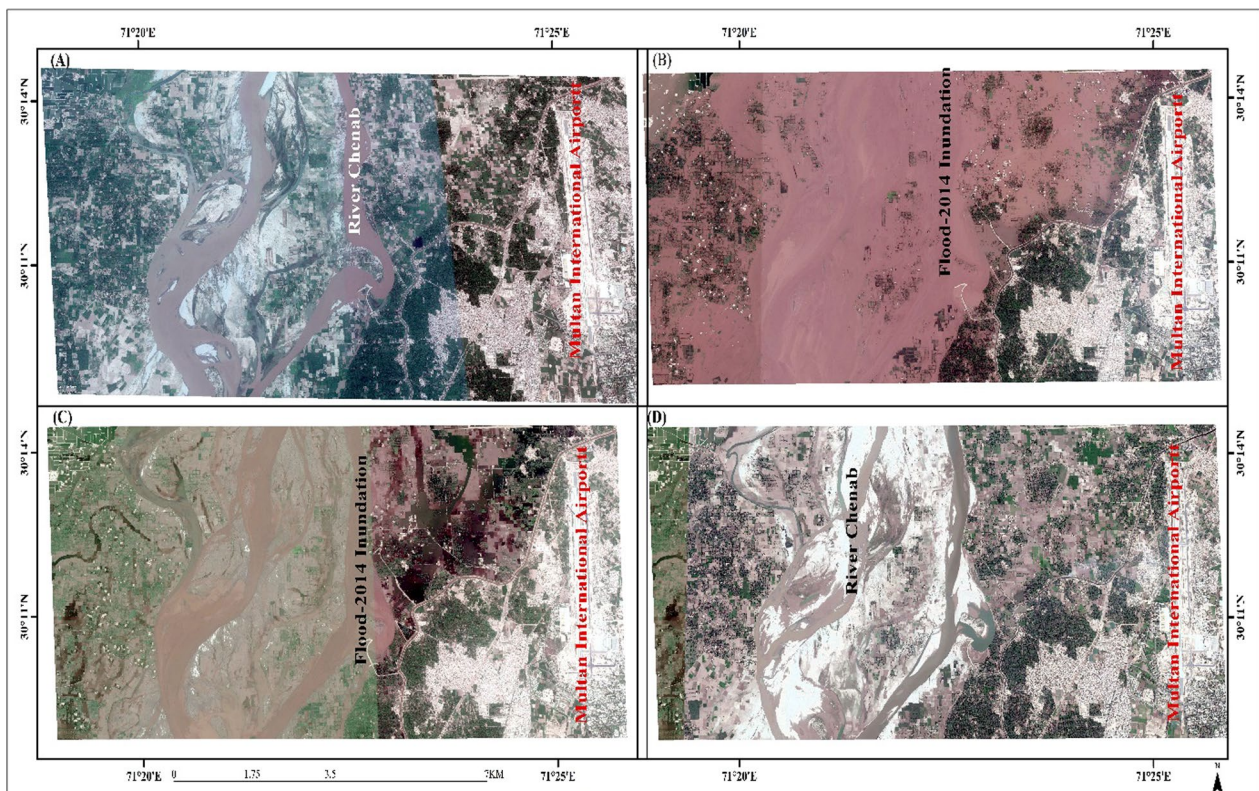
Fig. 7 Google Earth Pro 7.3.3.7786 images in the studied area, **A** 4th August,2014 **B** 18th September, 2014, **C** 1st October, 2014, **D** 11th November, 2014.Eye alt 11.42 mi

Table 4 Accuracy assessment of during flood Supervised LULC classification

Land use classes	During Flood classified image			
	User Accuracy	Producer Accuracy	Overall Accuracy	Kappa coefficient
Water areas	0.98	0.92	0.92	0.88
Built up areas	0.93	0.86		
Vegetation areas	0.94	0.89		
Barren area	0.99	0.85		
Sand areas	0.95	0.89		

inundation was overlaid and intersected to show misclassified areas by different water indices from 'non water' areas as well as 'water' areas. The results showed that NDWI misclassified barren and built-up areas while WRI misclassified vegetation areas and also did not identify shallow water areas that led to a lower overall accuracy level. The values are given in Table 5. We present the total water area extracted by each method in Table 5 and the misclassified areas in Table 6. We compare the extracted class using the classified image and the misclassified area in the water indices, with a supervised classified image as a reference point. For built-up areas, only 5.4 km^2 were

misclassified as water areas by MNDWI, compared with 30.4 and 39.1 km^2 for NDWI and WRI, respectively as listed in Table 5. The NDWI showed only 19.2 km^2 vegetation areas are misclassified as water areas, compared with 30.4 and 39.1 km^2 for MNDWI and WRI indices (Table 5). Moreover, the sand areas, about 2 km^2 were misclassified as water areas by WRI and MNDWI, compared with 18.1 km^{2}for NDWI. Similarly, the MNDWI and WRI showed about 1 km^2 barren land area was misclassified as water area, compared with 60 km^2 by NDWI. The comparison of results from all three indices shows that MNDWI shows a satisfactory result that can be

Sajjad *et al. Geoenvironmental Disasters*　　(2023) 10:9
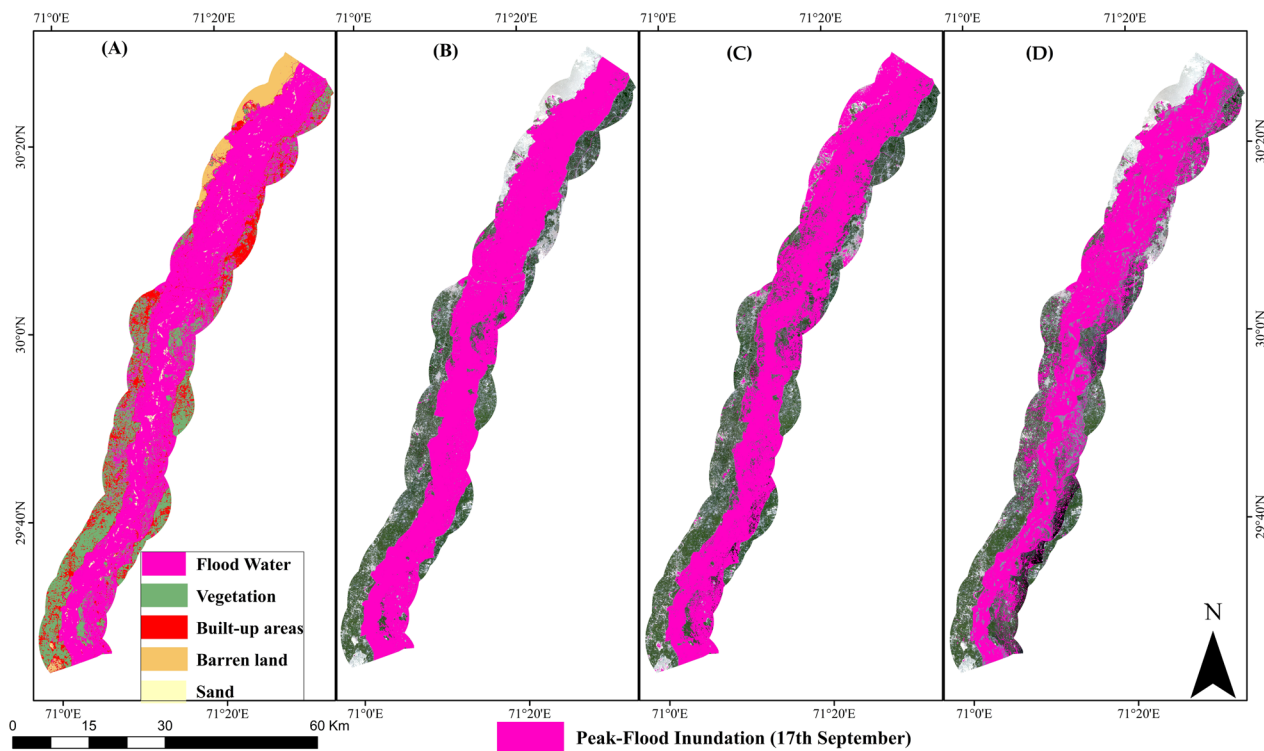
Page 12 of 18

Fig. 8 A. comparison of Peak-Flood-2014 Inundation using **A** Supervised Classification **B** MNDWI **C** NDWI and **D** WRI

used for flood mapping. The comparison uses the least misclassified areas for an index as the class in the final water classification. We also used during flood GE (18th September) image for comparing water indices results (Fig. 10B). Both maps show a similar pattern of comparison that NDWI misclassified built-up area as water area, in the eastern part. The MNDWI misclassified inundated vegetation as flooded areas in the western part of the study area. The WRI also classified more vegetation areas as flooded in the eastern and western part. In WRI image, the shallow flooded areas are not detected as seen in the GE comparison map. Such shallow flooded areas are identified as patches of water, in the central part, but

same areas were not detected as shallow flooded areas in WRI image. So the comparison of indices brings robust results and helps us to properly identify the most suitable water index for rapid flooded areas delineation in any area with similar type of mixed agriculture, built up, barren and sand landuses. Therefore, this study suggests that if the area has mixed Land uses, these indices can be used to complement each other in clearing the misclassified areas. Future researchers can utilized MNDWI index in this study area to asses flood extent and formulate flood management strategies in term of rescue and relief operations. The results also suggested that researcher can assess the appropriateness of other water indices while using LULC characteristics in order to extract flooded areas in other areas of the world. This approach would bring a new perspective in the flood monitoring using open satellite data awith techniques.
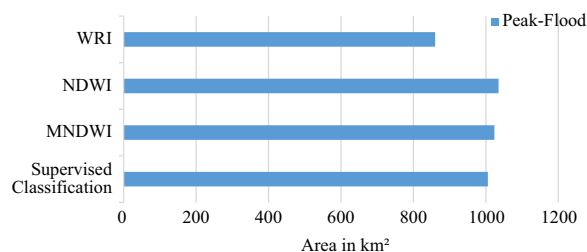
Discussion

Our results reveal that Landsat 8 images, together with satellite-derived MNDWI, NDWI and WRI indices permit the detailed flooded areas delineation with reliable accuracy. A recent review paper, similarly, analyszed and compared different indices used to depict area under flood water and regarded MNDWI to be the most suitable in terms of its ability to differentiate between turbid
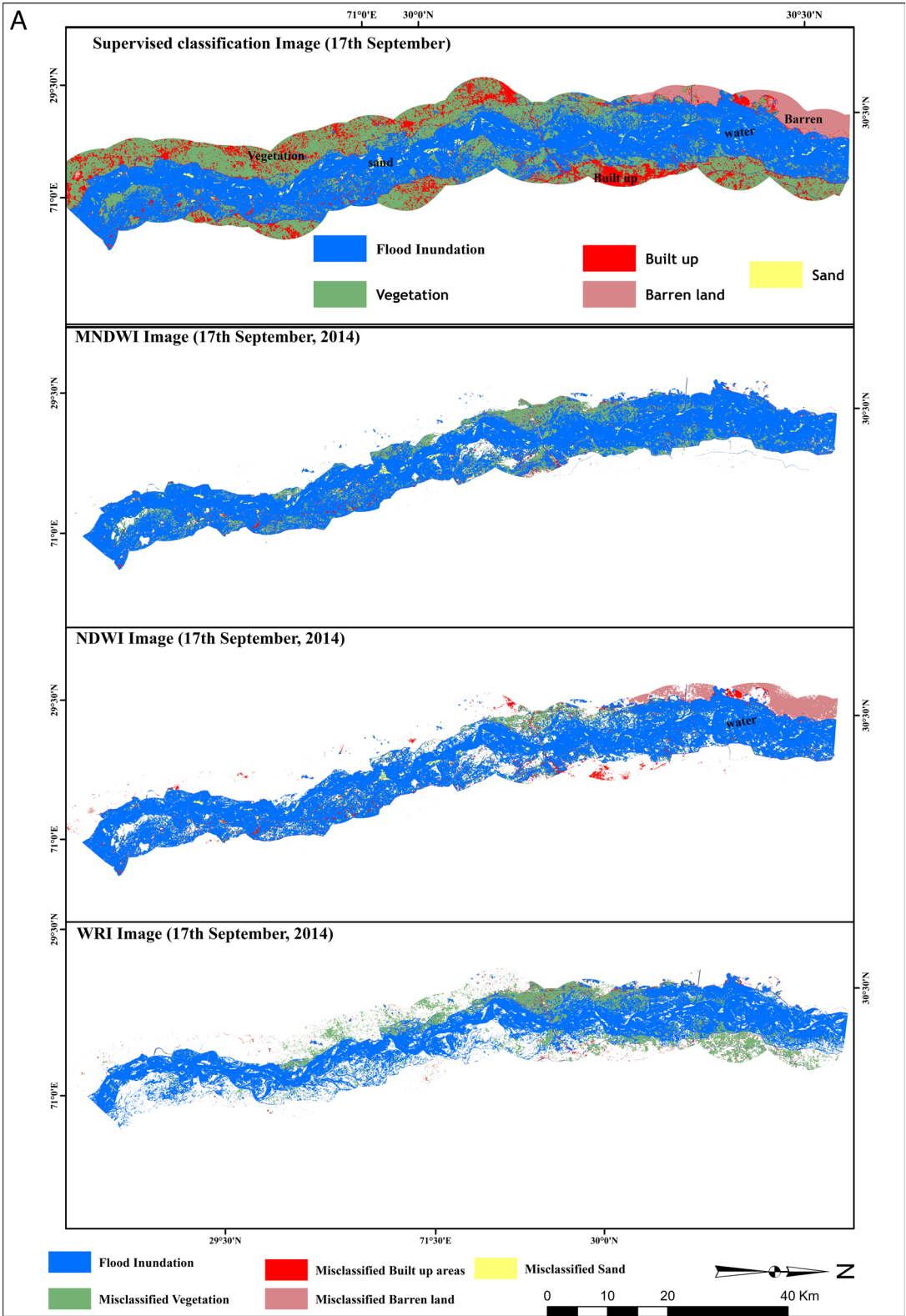

Fig. 9 A graph showing comparison of Peak-Flood-2014 Inundation using SC, MNDWI, NDWI, and WRI indices

Fig. 10 **A**. A comparison of Flood inundation using ML Classification, MNDWI, NDWI and WRI indices. **B**. A comparison of Flood inundation using GE, MNDWI, NDWI, and WRI indices
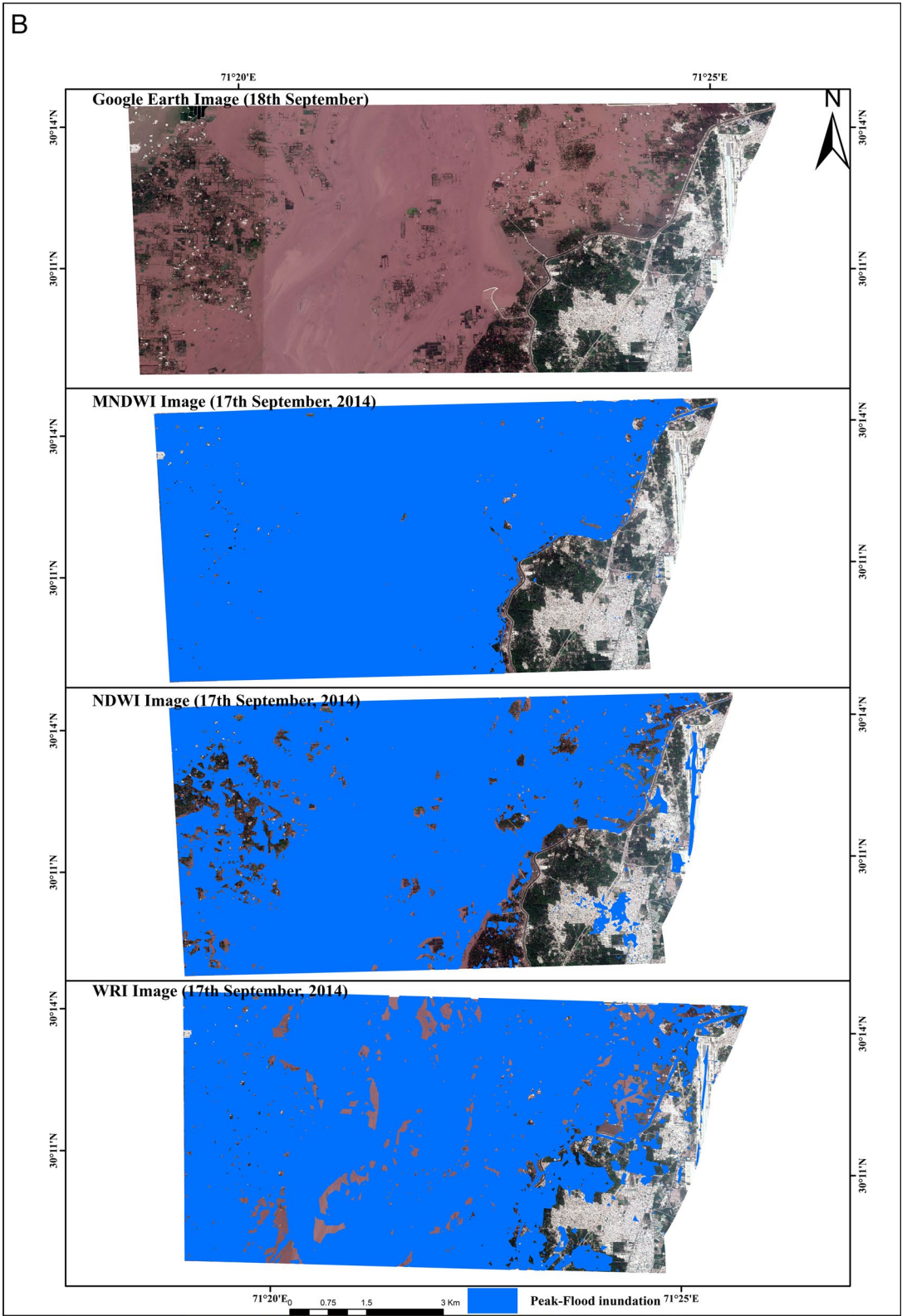
Fig. 10 continued

Table 5 Total flooded area extracted from different techniques

Total areas extracted by SC and indices

Land use classes	SC	MNDWI	NDWI	WRI
Water	1005.4	981.4	907.3	760.1
Built up	203.2	5.4	30.4	39.1
Vegetation	429.15	33.4	19.2	58.2
Sand	19.2	2.1	18.1	1.3
Barren	80.3	1.1	60.1	1.3
Total areas extracted by SC and Indices	1682.369	1023.4	1035.1	860

Table 6 Misclassified areas from indices based on the results from supervised classification

Misclassified areas in sq.km

	MNDWI	NDWI	WRI
Built up	5.4	30.4	39.1
Vegetation	33.4	19.2	58.2
Sand	2.1	18.1	1.3
Barren	1.1	60.1	1.3

water and mixed pixels (Albertini et al. 2022). The suitable satellite data is critical for RFM. Firstly, the temporal relationship between satellite characteristics with flood incidence is a vital parameter in RFM. For example, a low-resolution MODIS satellite (~ 250 m), with its rapid revisit time has been utilized during several floods to acquire a rapid flood inundation mapping, but with uncertain accuracy (Haq et al. 2012; Memon et al. 2015). However, due to the lack of during flood open high resolution satellite data, such as Sentinel-1,we employed multispectral Landsat data with a resolution of 30 m for rapid flood mapping (Bhatt et al. 2016; Notti et al. 2018). Albertini et al. (2022), in their recent review article also concluded Landsat to be most commonly used satellite for flood water spatial coverage detection. Despite the better spatial resolution, Landsat satellite data is constrained and cannot obtain geospatial data on time, which usually reduces its applicability for RFM (Mahmood et al. 2019; Sajjad et al. 2020). Our study area, however, is located between two close Landsat pathways (150 and 151), allowing for the capture of high-temporal resolution Landsat data (eight days), compared to a 15-day temporal resolution for an area (Shuhua et al. 2009; Mahmood et al. 2021). As a result of the high temporal resolution, we were able to conduct a thorough investigation of rapid flood mapping. Secondly, the capacity to acquire during flood images can be hampered by the presence of clouds in the sky. In comparison to optical multispectral

satellites such as MODIS and Landsat, SAR satellites can readily obtain RADAR images in any weather situations (Pradhan et al. 2009; Amitrano et al. 2018; Giordan et al. 2018). In our study, the SAR satellite data was not freely available and during the 2014 flood, the study area was fully cloud-free because the causal rainfall event occurred in upper Chenab (PMD 2014), about 10 days before the water reached the study area. Finally, the accuracy of mentioned indices to the satellite data was considered in order to determine the reliability of RFM. The MNDWI index has the highest overall accuracy of 97%, whereas the NDWI and WRI images have 92% and 89% overall accuracy, respectively (Table 2). The MNDWI index had achieved the highest overall accuracy of 97%, and has been efficiently used in other studies as well for detecting area under flood water (Guvel et al. 2022), while the NDWI and WRI images produce the highest overall accuracy of about 92% and 89% respectively (Table 1). Furthermore, the flood got reduced in three phases; in the first phase, floodwater receded with a rate of 10 km^2 per day, until 10th October. In the second moderate phase, the water significantly reduced until 26th October, with a decreasing rate of 17 km^2 per day. In the last phase, the water was reduced at the rate of 11 km^2 per day until 11th November, when Chenab river retained its before floodwater flow situation. These inundation results are endorsed by GE images, which also show the similar Spatio-temporal pattern of flood inundation with its phases as shown in Fig. 7.

In this study, for the identification of flooded areas, the peak flood (17th September) image was used as a reference, in order to evaluate and compare the result of water indices with supervised classified and GE images (Fisher et al. 2016). In our case, the MNDWI index produced better results, compared to NDWI and WRI indices, as shown in Figs. 8 and 9. Furthermore, the misclassification errors in the NDWI index images were revealed, due to mixed barren land areas with wet sand, and some built-up areas also misclassified as floodwater, mostly in the upper part of the study area. Moreover, the WRI index images show that the shallow water areas were not detected accurately, and wrongly detected some vegetation areas as water class, as a result, the low overall accuracy was attained, compared with MNDWI and NDWI indices (Figs. 8 and 10). The overall result shows that the satellite data obtained in the shortwave-Infrared (SWIR) wavelength can be useful for detecting flooded areas. Therefore, the MNDWI derived images show better results, as it slightly misclassifies water areas with vegetation class. On the basis of used water indices, the peak flood was identified on the 17th of September in the study area and then flood water persisted for seven weeks

Sajjad *et al. Geoenvironmental Disasters*   (2023) 10:9

Page 16 of 18

(Figs. 3, 4 and 5). The field survey also reveals a similar flood pattern, duration and recession (Sajjad et al. 2020).

Currently, the ~ 16-day temporal resolution of Landsat-8 data is a limiting factor for rapid flood inundation mapping for early flood response of an area. But, the launch of the Landsat-9 satellite in September 2021 have overcome this limitation, as the temporal resolution have been reduced to ~ 8 days. But in our case, the study area was overlapped by dual Landsat paths which allowed us to perform rapid flood mapping with ~ 8 days interval. The high temporal resolution can enhance the possibility of acquiring cloud-free Landsat satellite data for an area. In our study, cloud-free during and post-flood Landsat images were acquired as the rainfall phenomenon happened in upper regions. To overcome this issue, future research can collect and combine RS images from different satellites such as optical Landsat for pre-flood with SAR for post-flood. Combining RS images from different satellites will pose extra challenges due to contrasts in their informational characteristics. The spatial and spectral characteristics of each image could be diverse. But, combining images from distinctive satellite programs would enhance the chances of getting cloud-free during and post-flood images and provide up-graded information to flood response organizations. Furthermore, the opportunities of RADAR and optical datasets combination will enhance as frequent active sensors have been launched by many organisations. This will offer assistance to overcome the weather issues for some regions and result in RFM which is essential from an early flood management.

This research found that the NDWI index misclassified barren and built-up areas with floodwater, but MNDWI and WRI did not mix water areas with barren and built-up (Fig. 10). However, the MNDWI index misclassified wet vegetation areas as flooded areas (Figu 10B), but in contrast, NDWI shows better performance while extracting flood water in vegetation areas that you can see in Fig. 10B. Therefore, this study suggests that if the area has mixed LULC, these indices can be used to complement each other in clearing the misclassified areas. Future researchers can assess the appropriateness of other water indices in order to extract flooded areas in other areas of the world. But, some indices require spectral characteristics in other bands, which might not be accessible in most satellites' data. The satellite data obtained in the Shortwave-Infrared (SWIR) wavelength can be useful for detecting flooded areas. Therefore, the MNDWI images show better results and the results of the current study are in accordance with the findings of Sivanpillai et al. (2021), who also concluded that in comparison with NDWI, MNDWI presented with more accurate flood extent maps.

Conclusions

In this study, we offered accessible rapid riverine flood mapping and monitoring with the incorporation of optical RS flood instance images and suitable flood inundation processing indices. Specifically, we have used Landsat-8 satellite images and a comparison of different water indices, i.e. MNDWI, NDWI, and WRI indices, for rapid riverine flood mapping and monitoring. Our work proposed an approach of comparing the results of these indices to minimize the misclassified water areas. This is in addition to the fact that these different water indices have been recognized to be suitable for rapid mapping of flooded areas in cloud free areas. Further, these water indices based technique is time-independent and provides almost instant results. The combination of water indices has the potential to contribute to reliable flood extent mapping using Landsat-8 data.

The analysis revealed that the MNDWI index derived images showed an accuracy of above 90%, which reflects the reliability of results, while the rapid flood images determined by NDWI and WRI indices, showed less accuracy level. The water indices based analysis revealed that floodwater covered about 68% of the study area, mostly in the north and central parts. The analysis further revealed that floodwater remained for about seven weeks. Despite the fact that riverine flooding is a frequent phenomenon, our study shows that the optical open satellite dataset and satellite-derived water indices can be suitable for rapid flood mapping and monitoring to articulate emergency flood response activities, mainly for recovery and relief operations.

Despite the research being local to Pakistan, the proposed approach can be extended to global perspectives on flooding. Using Landsat imagery, and comparing satellite-derived water indices had led to the precise mapping of flooded areas and showed robust results, matching with field survey findings. Furthermore, the field visit helped us to investigate real-time spatial rapid flood mapping in the study area. Moreover, the study identified areas with mixed land use and land cover for better delineation of the flooded area using a least misclassified area approach. For instance, the misclassified built-up areas covered only 5.4 square kilometer for MNDWI, compared to 30.4 and 39.1 square kilometers for NDWI and WRI, respectively. For vegetation, NDWI had a least misclassified area of 19.5 square kilometers, compared to 33.4 square kilometers and 52.4 square kilo-meters for MNDWI and WRI, respectively. Similarly, the MNDWI and WRI showed about 1 square kilometer barren land area was misclassified as water areas, compared with 60 square kilometers by NDWI. Furthermore, we have also revealed that the exploitation of two nearby Landsat overlapping satellite paths enhances

Sajjad *et al. Geoenvironmental Disasters*   (2023) 10:9

Page 17 of 18

the temporal resolution of Landsat data from ~ 16 days to ~ 8 days that can be utilized for rapid flood mapping for emergency response operations. Therefore, the rapid flood mapping strategy proposed here can be utilized for producing flood inundation maps based on pre, during and post-flood instance images for an area. Highlighting the newly flooded areas will enhance the response actions in targeted areas of flood emergency management organizations.

Author contributions
Conceptualized overall research design, SA, JL; image analysis, flood inundation maps, LULC maps, flood Impact assessment, SA; validation, SA, JL, CC. SM; investigation, CX, writing—original draft preparation, SA; writing—review and editing, SA, JL, SM, NM. All authors read and approved the final manuscript.

Availability of data and materials
The datasets used and/or analysed during the current study are available from the corresponding author on reasonable request.

Declarations

Ethics approval and consent to participate.
Not applicable.

Consent for publication
Not applicable.

Competing interests
The authors declare that they have no competing interests.

References
Acharya TD, Subedi A, Yang IT, Lee DH (2018) Combining water indices for water and background threshold in Landsat image. Proceedings 2: 143

Albertini C, Gioia A, Iacobellis V, Manfreda S (2022) Detection of surface water and floods with multispectral satellites. Remote Sens 14(23):6005

AlFaisal A, Kafy AA, Roy S (2018) Integration of remote sensing and GIS techniques for flood monitoring and damage assessment: a case study of Naogaon District, Bangladesh. J Remote Sens GIS 7:236

Alphan H, Doygun H, Unlukaplan YI (2009) Postclassification comparison of land cover using multitemporal Landsat and ASTER imagery: the case of Kahramanmaras, Turkey. Environ Monit Assess 151:327–336

Amitrano D, Martino GD, Iodice A, Riccio D, Ruello G (2018) Unsupervised rapid flood mapping using Sentinel-1 GRD SAR images. IEEE Trans Geosci Remote Sens 56(6):3290–3299

Arnell NW, Gosling SN (2016) The impacts of climate change on river flood risk at the global scale. Clim Change 134:387

Bhatt CM, Rao GS, Farooq M, Manjusree P, Shukla A, Sharma SVSP, Kulkarni SS, Begum A, Bhanumurthy V, Diwakar PG, Dadhwal VK (2016) Satellite-based assessment of the catastrophic Jhelum floods of September 2014, Jammu & Kashmir, India. Geomatics. Nat Hazards Risk 8:309–327

Boni G, Ferraris L, Pulvirenti L, Squicciarino G, Pierdicca N, Candela L, Pisani AR, Zoffoli S, Onori R, Proietti C, Pagliara PA (2016) Prototype system for flood monitoring based on flood forecast combined with COSMO-SkyMed and Sentinel-1 Data. IEEE J Sel Top Appl Earth Obs Remote Sens 9(6):2794–2805

Borah SB, Sivasankar T, Ramya M, Raju P (2018) Flood inundation mapping and monitoring in Kaziranga National Park, Assam using Sentinel-1 SAR data. Environ Monit Assess 190:520

Chavez PS Jr (1996) Image-based atmospheric corrections—revisited and improved. Photogramm Eng Remote Sens 62:1025–1036

Federal Flood Commission Islamabad (FFCI) (2014) Annual flood report. Ministry of Water and Power, Pakistan

Fisher A, Flood N, Danaher T (2016) Comparing Landsat water index methods for automated water classification in eastern Australia. Remote Sens Environ 175:167–182

Gao W, Shen Q, Zhou Y, Li X (2018) Analysis of flood inundation in ungauged basins based on multi-source remote sensing data. Environ Monit Assess 190(3):129

Giordan D, Notti D, Villa A, Zucca F, Calò F, Pepe A, Dutto F, Pari P, Baldo M, Allasia P (2018) Low cost, multiscale and multi-sensor application for flooded area mapping. Nat Hazards Earth Syst Sci 18:1493–1516

Goffi A, Stroppiana D, Brivio PA, Bordogna G, Boschetti M (2020) Towards an automated approach to map flooded areas from Sentinel-2 MSI data and soft integration of water spectral features. Int J Appl Earth Obs Geoinf 84:101951

Güvel ŞP, Akgül MA, Aksu H (2022) Flood inundation maps using Sentinel-2: a case study in Berdan Plain. Water Supply 22(4):4098–4108

Haq M, Akhtar M, Muhammad S, Paras S, Rahmatullah J (2012) Techniques of Remote Sensing and GIS for flood monitoring and damage assessment: a case study of Sindh province, Pakistan. Egypt J Rem Sens Space Sci 15:135–141

Hu Q, Wu W, Xia T, Yu Q, Yang P, Li Z, Song Q (2013) Exploring the use of Google Earth imagery and object-based methods in land use/cover mapping. Remote Sens 5:6026–6042

Islam AS, Bala SK, Haque M (2010) Flood inundation map of Bangladesh using MODIS time-series images. J Flood Risk Manag 3:210–222

Joyce KE, Belliss SE, Samsonov SV, McNeill SJ, Glassey PJ (2009) A review of the status of satellite remote sensing and image processing techniques for mapping natural hazards and disasters. Prog Phys Geogr 33:183–207

Kaku K, Aso N, Takiguchi F (2015) Space-based response to the 2011 great east Japan earthquake: lessons learnt from JAXA's support using earth observation satellites. Int J Disaster Risk Reduct 12:134–153

Khalid B, Cholaw B, Alvim DS, Javeed S, Khan JA, Javed MA, Khan AH (2018) Riverine flood assessment in Jhang district in connection with ENSO and summer monsoon rainfall over Upper Indus Basin for 2010. Nat Hazards 92:971–993

Kundzewicz ZW, Kanae S, Seneviratne SI, Handmer J, Nicholls N, Peduzzi P, Mechler R, Bouwer LM, Arnell N, Mach K (2014) Flood risk and climate change: global and regional perspectives. Hydrol Sci J 59:1–28

Mahmood S, Rani R (2022) People-centric geo-spatial exposure and damage assessment of 2014 flood in lower Chenab Basin, upper Indus Plain in Pakistan. Nat Hazards 111:3053–3069. https://doi.org/10.1007/s11069-021-05167-w

Mahmood S, Sajjad A, Rahman A (2021) Cause and damage analysis of 2010 flood disaster in district Muzaffar Garh, Pakistan. Nat Hazards. https://doi.org/10.1007/s11069-021-04652-6

Mahmood S, Rahman A, Sajjad A (2019) Assessment of 2010 flood disaster causes and damages in district Muzaffargarh, Central Indus Basin. Pak Environ Earth Sci 78:63

Manavalan R (2017) SAR image analysis techniques for flood area mapping - literature survey. Earth Sci Inf 10(1):1–14

Manjusree P, Prasanna KL, Bhatt CM, Rao GS, Bhanumurthy V (2012) Optimization of threshold ranges for rapid flood inundation mapping by evaluating backscatter profiles of high incidence angle SAR images. Int J Disaster Risk Sci 3(2):113–122

McFeeters SK (1996) The use of the normalized difference water index (NDWI) in the delineation of open water features. Int J Remote Sens 17:1425–1432

Memon AA, Muhammad S, Rahman S, Haq M (2015) Flood monitoring and damage assessment using water indices: a case study of Pakistan flood-2012. Egypt J Remote Sens Space Sci 18:99–106

Munasinghe D, Cohen S, Huang YF, Tsang YP, Zhang J, Fang ZF (2018) Intercomparison of satellite remote sensing-based flood inundation mapping techniques. J Am Water Resour Assoc 54:834–846

Sajjad *et al. Geoenvironmental Disasters*   (2023) 10:9

Page 18 of 18

Notti D, Giordan D, Caló F, Pepe A, Zucca F, Pedro Galve J (2018) Potential and limitations of open satellite data for flood mapping. Remote Sens 10:1–30

PMD (Pakistan Meteorological Department) (2014)Annual Report; Regional Meteorological Observatory: Lahore, Pakistan

Pradhan B, Pirasteh S, Shafie M (2009) Maximum flood prone area mapping using RADARSAT images and GIS: Kelantan river basin. Int J Geoinformatics 5:11–23

Rahman MR, Thakur PK (2017) Detecting, mapping and analyzing of flood water propagation using synthetic aperture radar (SAR) satellite data and GIS: a case study from the Kendrapara district of Orissa state of India. Egypt J Remote Sens Space Sci 21:537–541

Refice A, Capolongo D, Pasquariello G, D'AddabboA BF, Nutricato R, Lovergine FP, Pietranera L (2014) SAR and InSAR for flood monitoring: examples with COSMO-SkyMed data. IEEE J Sel Top Appl Earth Obs Remote Sens 7(7):2711–2722

Revilla-Romero B, Hirpa FA, Pozo JT, Salamon P, Brakenridge R, Pappenberger F, De Groeve T (2015) On the use of global flood forecasts and satellite-derived inundation maps for flood monitoring in data-sparse regions. Remote Sens 7:15702–15728

Rokni K, Ahmad A, Selamat A, Hazini S (2014) Water feature extraction and change detection using multitemporal Landsat imagery. Remote Sens 6:4173–4189

Rosser JF, Leibovici DG, Jackson MJ (2017) Rapid flood inundation mapping using social media, remote sensing and topographic data. Nat Hazards 87(1):103–120

Sajjad A, Lu J, Chen X, Chisenga C, Mahmood S (2019) The riverine flood catastrophe in august 2010 in south Punjab, Pakistan: potential causes, extent and damage assessment. Appl Ecol Environ Res 17(6):14121–14142

Sajjad A, Lu J, Chen X, Chisenga C, Saleem N, Hassan H (2020) operational monitoring and damage assessment of riverine Flood-2014 in the lower Chenab Plain, Punjab, Pakistan, using remote sensing and GIS techniques. Remote Sens 12:714

Sajjad A, Lu J, Chen X, Chisenga C, Mazhar N, Nadeem B (2021) Riverine flood mapping and impact assessment using remote sensing technique: a case study of Chenab flood-2014 in Multan district, Punjab, Pakistan. Nat Hazards 110:2207–2226

Sanyal J, Lu XX (2004) Application of remote sensing in flood management with special reference to Monsoon Asia: a review. Nat Hazards 33:283–301

Shen I, Li C (2010) Water body extraction from Landsat ETM+ imagery using adaboost algorithm. In: IEEE. 2010 18th International Conference on Geoinformatics; Beijing 18–20: 1–4

Shuhua QI, Brown DG, Tian Q, Jiang L, Zhao T, Bergen KM (2009) Inundation extent and flood frequency mapping using LANDSAT imagery and digital elevation models. Giscience Remote Sens 46:101–127

Sivanpillai R, Jacobs KM, Mattilio CM, Piskorski EV (2021) Rapid flood inundation mapping by differencing water indices from pre and post flood Landsat images. Front Earth Sci 15:1–11

Uddin K, Matin MA, Meyer FJ (2019) Operational flood mapping using multi-temporal sentinel-1 SAR images: a case study from Bangladesh. Remote Sens 11:1581

Wulder MA, Masek JG, CohenWB LTR, Woodcock CE (2012) Opening the archive: how free data has enabled the science and monitoring promise of Landsat. Remote Sens Environ 12:2–10

Xu H (2006) Modification of normalized difference water index (NDWI) to enhance open water features in remotely sensed imagery. Int J Remote Sens 27:3025–3033

Zhang P, Lu J, Feng L, Chen X, Zhang L, Xiao X, Liu H (2015) Hydrodynamic and inundation modeling of china's largest freshwater lake aided by remote sensing data. Remote Sens 7:4858–4879

Publisher's Note

Springer Nature remains neutral with regard to jurisdictional claims in published maps and institutional affiliations.